Simulations of a micro-PET System based on Liquid Xenon

A. Miceli[1], J. Glister[1], A. Andreyev [2], D. Bryman[2], L. Kurchaninov[1], P. Lu[1], A. Muennich[1], F. Retiere[1], and V. Sossi[2]

[1] TRIUMF, 4004 Wesbrook Mall, Vancouver V6T 2A3, Canada

[2] Department of Physics and Astronomy, University of British Columbia, 6224 Agricultural Road, Vancouver V6T 1Z1, Canada

Abstract. The imaging performance of a high-resolution preclinical PET system employing liquid xenon as the gamma ray detection medium was simulated. The arrangment comprises a ring of detectors consisting of trapezoidal LXe time projection ionization chambers and two arrays of large area avalanche photodiodes for the measurement of ionization charge and scintillation light. A key feature of the LXePET system is the ability to identify individual photon interactions with high energy resolution and high spatial resolution in 3 dimensions and determine the correct interaction sequence using Compton reconstruction algorithms. The simulated LXePET imaging performance was evaluated by computing the noise equivalent count rate, the sensitivity and point spread function for a point source, and by examining the image quality using a micro-Derenzo phantom according to the NEMA-NU4 standard. Results of these simulation studies included NECR peaking at 1372 kcps at 262 MBq (712 kcps at 192 MBq) for an energy window of 450 - 600 keV and a coincidence window of 1 ns for mouse (rat) phantoms. The absolute sensitivity at the center of the field of view was 12.6%. Radial, tangential, and axial resolutions of ^{22}Na point sources reconstructed with a list-mode maximum likelihood expectation maximization algorithm were ≤ 0.8 mm (FWHM) throughout the field of view. Hot-rod inserts of $<$ 0.8 mm diameter were resolvable in the transaxial image of a micro-Derenzo phantom. The simulations show that a liquid xenon system would provide new capabilities for significantly enhancing PET images.

1. Introduction

Positron Emission Tomography (PET) is a functional medical imaging technique of increasing importance. Its power resides in the ability to investigate biological processes that are altered by disease and to trace radio-labeled molecules in organs. PET imaging can be used for early cancer screening, studying the pathology of illness, and to guide the development of new drugs.

Recently, several efforts were made to improve the sensitivity and spatial resolution of preclinical PET scanners by developing scintillation crystal-based detectors capable of measuring depth of interaction [1–3].

We are developing a novel high-resolution preclinical PET system using ionization and scintillation light signals from gamma ray interactions in liquid xenon (LXe). The Time Projection Chamber (TPC) [4] configuration is employed where ionization electrons are collected without gain on electrodes after drifting 11 cm under an applied electric field of 1-3 kV/cm. Ionization from photon interactions can be localized in 3-D to < 1 mm because electron diffusion is small in LXe. Low diffusion also allows separation of individual photon interactions. Charge collection efficiency is high as long as the level of impurities in the LXe is sufficiently low (ppb level) [5,6]. Photon interactions also produce copious scintillation light in LXe (68000 photons/MeV at zero electric field) with time constants of 2.2 ns and 27 ns, which is detected in our set-up by a set of Large Area Avalanche Photo-diodes (LAAPD) [7]; scintillation light is used to measure the interaction time with high resolution and contributes to the energy measurement. Furthermore, using both charge and scintillation light, excellent energy resolution (< 4% FWHM at 662 keV) has been reported [8].

LXe can be used to cover large detection volumes with high uniformity over the entire field of view (FOV) improving the detection sensitivity. Our previous studies on the use of LXe as a detection medium in PET were reported in [9]. In this paper, we describe a simulation of a LXe μ-PET scanner and the Compton reconstruction algorithm developed for sequencing multi-interaction events. In addition, we present the simulated imaging performance of the LXePET system including sensitivity, scatter fraction, spatial resolution, and image quality evaluated according to the NEMA standard NU4 [10].

2. Simulation Framework

2.1. Simulation model

Figure 1 shows the LXePET scanner consisting of twelve trapezoidal sectors arranged in a ring geometry. The inner bore has 10 cm dia. and 10 cm axial length. The liquid xenon is contained in a stainless-steel vessel thermally insulated by a vacuum space. Each sector is a LXeTPC viewed by two arrays of LAAPDs. The anode and cathode areas are 10 cm x 9.2 cm and 10 cm x 3.2 cm, respectively, and the drift length is 11.2 cm. Each APD array consists of 7 APDs with 16 mm dia., 9 APDs with 10 mm dia.,

and 8 APDs with 5 mm dia. Smaller APDs are used in the inner region to enhance the reconstruction where most of the events occur. Figure 2 shows the APD layout in one of the sectors.
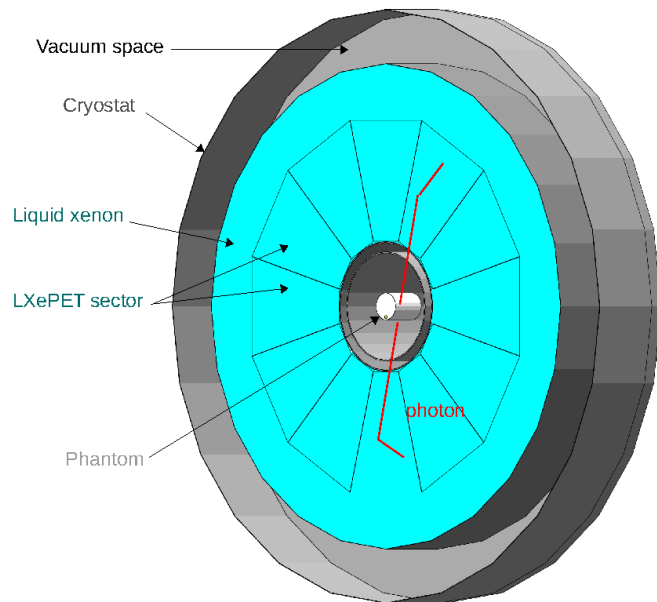

Figure 1: Simulated LXe PET system. The Cryostat, LXePET sectors, inner vessel filled with LXe (blue), and mouse-like NEMA phantom are illustrated. The red lines indicate a pair of annihilation photons which interact in the LXe.
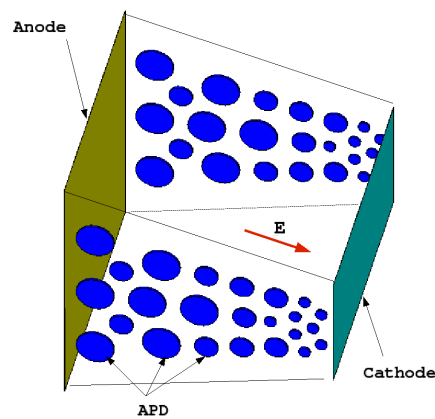

Figure 2: APD layout in one of the LXePET sectors.

The simulation of the LXe prototype was carried out with the Geant4 simulation package [11]. A positron emitter (^{18}F or ^{22}Na depending on the study) was simulated. Following the decay of the radioisotope, positrons with energy sampled from a continuous distribution of the beta decay process were generated and tracked until annihilation. To simulate the non-colinearity of the annihilation photons a new

process was created and integrated in Geant4. The new process simulates the positron annihilation in flight according to the Geant4 annihilation process and replaces the Geant4 annihilation at rest with a model where the non-zero momentum of the electron-positron pair is taken into account. The interaction of the annihilation photons with the phantom and PET scanner was simulated with the low energy package of Geant4. Energy and 3D position of every photon interaction in the LXe detector were recorded. The numbers of ionization charges N_{e-}^i and scintillation photons S_i created in the interactions were calculated as [12]:

$$N_{e-}^i = \frac{(1 - Fr^*) \times E_i^{G4}}{15.6eV} \tag{1}$$

$$S^i = \frac{(SF + Fr^*) \times E_i^{G4}}{15.6eV} \tag{2}$$

where Fr* is the electron-ion recombination fraction, E_i^{G4} is the energy deposited in the interaction i and SF = 0.2 [8] is the ratio of the number of excitons and ion pairs produced. The electron-ion recombination fraction Fr* varies on an event-by-event basis. It was modeled as a Gaussian function centered at Fr = 0.24 with width $\Delta Fr = 0.032$ [9]. Electronics and photo-detectors were not simulated directly. Instead, instrumental responses were parameterized in subsequent analyses as described in [12]. The parameters used in the simulation are listed in Table 1.

Following the National Electrical Manufacturers Association (NEMA) standards [10], four phantoms were simulated, depending on the study being performed. The first was a point source (diameter 0.25 mm) of the radionuclide ^{22}Na embedded in an acrylic cube of 10.0 mm extent on all sides. The second (third) was a rat (mouse)-like phantom consisting of a 50(25) mm dia. and 150(70) mm length polyethylene cylinder with a 3.2 mm dia. hole drilled at a radial distance of 17.5(10) mm. A 3.2 mm dia. 140(60) mm long rod was filled with water and the radionuclide ^{18}F. The point source was used for sensitivity and resolution studies while the mouse and rat phantoms were used for count rate studies. The last phantom was a micro-Derenzo phantom used to assess the quality of image reconstruction. It was made from acrylic and measured 40 mm in dia. and 35 mm in length. Arrayed throughout the phantom were cylindrical rods of length 30 mm and diameters 1.6, 1.4, 1.2, 1.0, 0.8 and 0.6 mm. The rods were offset radially by 7 mm from the phantom center and filled with water and ^{18}F. The rod-to-rod separation was set to twice the rod diameter.

2.2. Event Selection

Coincidence events were selected using a two-step procedure. The first stage of the event selection simulated the response of the detector trigger using only the information from the scintillation light. Events producing less than 5000 scintillation photons (corresponding to approximately 180 keV) were rejected. For each photon of each annihilation pair passing the first selection stage, we calculated the energy from the scintillation light corrected for the solid angle using the information of the position

Table 1: Simulation parameters.

Recombination factor	Fr	0.24
Fluctuation of the e-ion recombination	ΔFr	0.032
Position resolution	σ_{pos}	0.3 mm
Minimum two-hits separation distance	d	1 mm
Electronic noise charge (APD 16mm)	ENC_A^{16}	5000 e-
Electronic noise charge (APD 10mm)	ENC_A^{10}	2000 e-
Electronic noise charge (APD 5mm)	ENC_A^{5}	500 e-
APD quantum efficiency	QE	80%
APD gain	G	500
APD excess noise factor	F	2.5
TPC electronic noise	ENC_Q	600 e-
Charge detection threshold	T_C	1800 e-

from the charge measurement [12] and we used the resulting value to calculate the light-charge combined energy as described in [8]. Events with combined energy 450-600 keV were kept. The first interaction points defining the lines of response (LOR) of the selected events were stored in a list-mode format. The Compton reconstruction algorithm described in section 2.3 was used to find the first interaction point for multi-sites events.

2.3. Compton Reconstruction Algorithm

When a photon interacts in the detector, it can Compton scatter multiple times before being photo-absorbed. A 511 keV photon is roughly three times more likely to Compton scatter than be photo-absorbed when it first interacts in LXe. The simplest interaction configuration is the 1-1 case in which the detector registers only 1 discernible interaction point for each of the two photons, corresponding to photo-absorption without scattering. Practically, however, multi-hit scenarios such as 1-2, 1-3, 2-2, etc. are more common, and must be taken into account, as they contribute to blurring of the image due to ambiguity in the location of the first interaction point. The goal of the Compton reconstruction algorithm is to sort through all the possible scattering sequences, determine the path that is the most probable, and define the most likely first interaction point and its associated line of response.

For each pair of photons interacting $M - N$ times in the detector, with M representing photon 1 and N photon 2, and $M \leq N$, there are $M!N!$ number of possible interaction sequences. For each sequence, a LOR check is first performed, determining whether the trajectory passes through the phantom. Then, if the sequence was found to be viable, Compton kinematics were used to compute a test statistic score associated with the sequence.

The Klein-Nishina formula determines the scattering angle based on the energy deposited:

$$\cos(\theta_E) = 1 + mc^2 \times (E_{\gamma i}^{-1} - E_{\gamma i+1}^{-1}) \tag{3}$$

where $E_{\gamma i}$ is the photon energy before the ith step given by:

$$E_{\gamma i} = E_{\gamma 1} - \sum_{j=1}^{i-1} dE_j, \qquad (4)$$

m is the electron mass, θ_E is the Compton scattering angle, dE_j is the energy deposited at the jth step, and $E_{\gamma 1} = 511$ keV is the energy of the photon before it reaches the detector. Alternatively, the scattering angle θ_G based on the position of interaction site is calculated as:

$$\cos(\theta_G) = \frac{\vec{u_i} \cdot \vec{u_{i+1}}}{|\vec{u_i}||\vec{u_{i+1}}|} \qquad (5)$$

where $\vec{u_i} = (x_i - x_{i-1}, y_i - y_{i-1}, z_i - z_{i-1})$.

For each candidate interaction site, we could, in principle, determine if the sequence was the correct one by comparing the scattering angles computed using the energy deposited (θ_E) with the observed scattering angles given the geometric distribution of interaction sites (θ_G). In the ideal situation, the difference would be zero.

The ability to resolve the correct sequence, however, depends on the position and energy resolution of the system. A statistical weighting was used to account for instrumental resolution limits:

$$\chi^2 = \sum_{i=1}^{N-1} \frac{(\cos(\theta_E)_i - \cos(\theta_G)_i)^2}{\Delta \cos(\theta_E)_i^2 + \Delta \cos(\theta_G)_i^2} \qquad (6)$$

where the error terms are defined as [13]:

$$\Delta cos(\theta_E)_i^2 = m^2 c^4 \times \left(\frac{\sigma_{dE_i}^2}{E_{\gamma i}^4} + \sigma_{E\gamma i+1}^2 \times (E_{\gamma i}^{-2} - E_{\gamma i+1}^{-2})^2 \right) \qquad (7)$$

and

$$\Delta cos(\theta_G)_i^2 = \sigma_{pos}^2 \times (\sigma g_{i,x} + \sigma g_{i,y} + \sigma g_{i,z}) \qquad (8)$$

where

$$\sigma \vec{g}_i = \left(\frac{\vec{u_{i+1}}}{|\vec{u_i}| \cdot |\vec{u_{i+1}}|} - \frac{\vec{u_i} \times cos(\theta_G)}{|\vec{u_i}|^2} \right)^2 + \left(\frac{\vec{u_i}}{|\vec{u_i}| \cdot |\vec{u_{i+1}}|} - \frac{\vec{u_{i+1}} \times cos(\theta_G)}{|\vec{u_{i+1}}|^2} \right)^2 \qquad (9)$$

The error on the energy deposited at the ith step, σ_{dE_i}, and the error on the photon energy after the interaction step i, $\sigma_{E\gamma i+1}$, are given by:

$$\sigma_{dE_i}^2 = ENC_Q^2 + \Delta Fr^2 \times dE_i^2 \qquad (10)$$

$$\sigma_{E\gamma i+1}^2 = i \times ENC_Q^2 + \Delta Fr^2 \times \sum_{j=1}^{i} dE_j^2 \qquad (11)$$

Finally, the viable sequence with the lowest test statistic score was chosen by the reconstruction algorithm, and the associated LOR defined and recorded. If no suitable interaction sequence was found, the event was discarded. This reconstruction technique is similar to the one used in [13, 14] modified for PET applications.

2.4. Detection Rate Calculation

The output of the simulation consisted of interaction steps for two types of events: singles where only one of the two photons interacted with the detector and double events where both photons reached the detector. These data are source activity independent and do not contain random coincidence events. In order to simulate the count rate performance of the LXe detector, the detection rates at different source activities and instrumental parameters, such as dead time and coincidence window, had to be calculated.

The calculation of detection rates was done via Poisson statistical modeling, taking into account the probability of each interaction type, and assuming that only events with exactly two photons detected were selected. Given the trigger probabilities of detecting zero (P_0), one (P_1), and two (P_2) photons from annihilation, the trigger rates for true and scatter events $C_{2,0}$ and for random events $C_{2r,0}$ for a given source activity, A, and coincidence window, Δt, can be computed:

$$C_{2,0}(A) = \frac{1}{\Delta t} \sum_{k=1}^{\infty} \frac{e^{-\lambda}\lambda^k}{k!} P_2 P_0^{k-1}, where\ \lambda = A * \Delta t\ and \tag{12}$$

$$C_{2r,0}(A) = \frac{1}{\Delta t} \sum_{k=2}^{\infty} \frac{e^{-\lambda}\lambda^k}{k!} P_1^2 P_0^{k-2} \tag{13}$$

Coincidence windows of 1, 3, and 6 ns were used in these studies. The count rate for true and scatter events $C_2(A)$ and for randoms $C_{2r}(A)$ are calculated as:

$$C_2(A) = \frac{C_{2,0}}{1 + C_{total,0}\tau}\epsilon_2, \tag{14}$$

$$C_{2r}(A) = \frac{C_{2r,0}}{1 + C_{total,0}\tau}\epsilon_{2r} \tag{15}$$

where τ is the instrumental dead time, and ϵ_2 and ϵ_{2r} are the probabilities of a triggered event to pass the event selection. $C_{total,0}$ is the total trigger rate including random coincidences. The ratios ϵ_2 and ϵ_{2r} depend on the combined energy resolution and energy window threshold, as well as the event reconstruction strategy used. They are calculated for each data set (simulated true plus scatter data set and random data set) as the number of events which have combined energy within the 450-600 keV energy window and define a LOR which passes through the phantom, divided by the number of triggered events. The random set was generated combining single unrelated events in pairs. The first stage trigger probabilities for zero, one, two photons detection, and 2nd-stage event selection efficiencies are given in Table 2. The trigger probability of detecting one or two photons is 60% for both the mouse and rat phantoms. The probability of detecting two photons depositing more than 180 keV is 22%, significantly higher for the mouse phantom than 13% found for the rat phantom due to the smaller amount of scattering produced by the mouse phantom. The size of the phantom is related to the amount of scattering produced, therefore to the probability of a triggered event to pass the event selection.

Table 2: Trigger probabilities for zero, one, two photons (P_0, P_1, P_2), and probabilities $(\epsilon_2, \epsilon_{2r})$ of a triggered event to pass the event selection for non-random and random events.

		Mouse-Like Phantom	Rat-Like Phantom
Scenario	$[P_0]$ (%)	41.5	40.8
	$[P_1]$ (%)	36.3	46.6
	$[P_2]$ (%)	22.2	12.6
Efficiency	ϵ_2 (%)	43.3	33.5
	ϵ_{2r} (%)	3.39	6.26

Once the two final detection rates were calculated, a rate dependence could be applied to the output of the Geant4 simulation. This was done by scaling the simulated double (true and scatter) and random events (pair-wise combinations of single events) to obtain the total detection rate $C_2(A) + C_{2r}(A)$. This scaling approach allowed us to use a single large set of simulation data to compute the behavior of the detector and its performance at various resolution limits and activities without the need to re-simulate under different detector parameters.

2.5. Image reconstruction

In order to preserve the high resolution spatial information contained in the data produced by the LXePET scanner, we reconstructed the point source data and the micro-Derenzo phantom with a list-mode reconstruction algorithm. The main advantage of the list-mode data reconstruction over the rebinned data reconstruction is improved and more uniform spatial resolution across the field-of-view. List-mode image reconstruction methods are also favorable in time-of-flight PET [15], motion corrected PET [16], and dynamic and gated PET [17]. We used a 3D list-mode image reconstruction algorithm for PET based on the maximum likelihood expectation maximization (MLEM) approach [18]. As in [19] and [20] each detected LOR was considered as a unique projection bin with the number of counts in each projection bin g_i equal to 1. Using notations f_j^n and f_j^{n+1} for the intensity vectors in voxel j for step n and the next $n + 1$ iteration estimates, the iteration step for the list-mode MLEM algorithm is equal to:

$$f_j^{n+1} = \frac{f_j^n}{s_j} \sum_i p_{ji} \frac{1}{\sum_k p_{ik} f_k^n} \tag{16}$$

where p_{ij} is the value of the system matrix describing the probability that a given emission event i originates from a certain voxel j, s_j is the sensitivity value for voxel j. The list-mode MLEM used *on-the-fly* ray-driven forward and-back projection with bilinear interpolation [21]. We used 20 MLEM iterations for the ^{22}Na point sources and 100 MLEM iterations for the Derenzo phantom. The voxel size was 0.15 x 0.15 x

0.15 mm and the image size was 360 x 360 x 360 voxels. The reconstruction time for point sources (5.5 million LORs on average) was less than 3 hours on an Intel Xeon 2.00 GHz CPU (single core). The reconstruction speed of the list-mode MLEM algorithm can be further improved by using the ordered subsets (OS) approach [22] and parallel processing.

3. Analysis

3.1. Sensitivity

Absolute sensitivity was calculated following the NEMA standard. A ^{22}Na point source was used for this study. The point source was stepped axially through the scanner at 0.5 mm steps over an axial length of 150 mm. One million ^{22}Na decays were simulated at each step. The absolute sensitivity at the center of the field of view (CFOV) for an energy window of [450,600] keV was 12.6 % . The sensitivity profile for all axial steps can be seen in Figure 3.
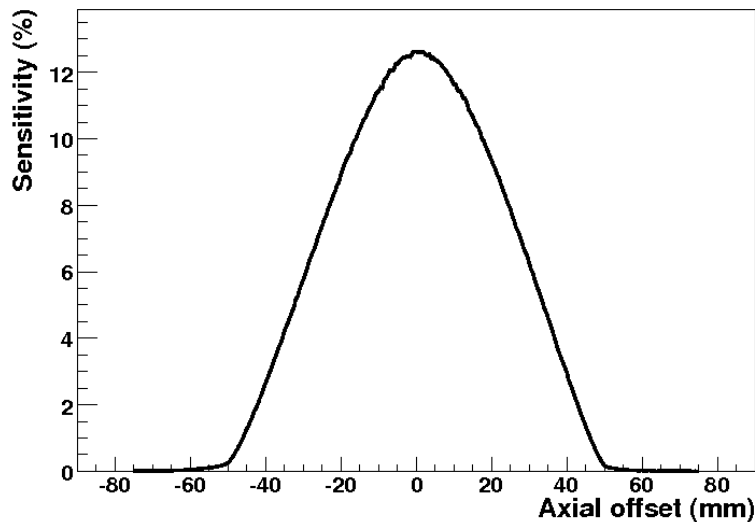

Figure 3: NEMA standard sensitivity profile for a ^{22}Na point source embedded in a 1 cm^3 acrylic cube, measured at 0.5 mm axial steps. Energy window: [450,600] keV.

3.2. Scatter Fraction and Count Rate Performance

The scatter fraction and noise equivalent count rate (NECR) studies were carried out using the rat-like and mouse-like phantoms following the NEMA protocol. For each phantom 50 million ^{18}F decays were simulated. The list-mode data were arranged in sinograms and oblique slices were combined into 2D projections using the SSRB method with a 1 cm slice thickness. Using a bin width of 0.3 mm, any radial pixel of the sinogram farther than 8 mm from the edges of the phantom was set to zero. For each projection

angle ϕ, the radial projection was shifted so that the maximum value was aligned with the central pixel of the sinogram. The pixels in each angular projection having the same radial offset were summed. Linear interpolation was used to find the pixel intensities at $\pm$ 7 mm from the central pixel location. The average of the two intensities was multiplied by the number of pixels between -7 mm and 7 mm. For each slice i, this value added to the counts outside the 14 mm central region and divided by the number of pairs in the data set defines the number of scattered event counts $C_{scatt,i}$. The total event count $C_{TOT,i}$ is the sum of the pixels in the projections divided by the number of pairs in the data set. No random events were added to the sinogram.

The scatter fraction is given by

$$SF = \sum_{i=1}^{NSlices} C_{scatt,i}/C_{TOT,i} \tag{17}$$

The mouse (rat) scatter fraction was 12.1%(20.8%), where 4.9% (10.5%) was due to scatter only and 7.2% (13.6%) was due to ambiguities in the Compton reconstruction algorithm. An example of Compton ambiguity involves multi-interaction events where one or both photons interact in only two locations and deposit the same amount of energy. To calculate the percentage of the scatter fraction due to Compton ambiguities we selected only true events in the simulation data set.

The random set was arranged in sinograms and oblique slices were combined into 2D projections using the SSRB method with a 1 cm slice thickness. The number of random counts $C_{random,i}$ for each slice was the total counts in the random coincidence sinogram within 8 mm from the edges of the phantom divided by the number of pairs in the random set.

The noise equivalent rate for each slice was calculated as follows, where $C_2(A)$ and $C_{2r}(A)$ are the rates previously calculated:

$$NECR_i(A) = \sum_{i=1}^{NSlices} \frac{((C_{TOT,i} - C_{scatt,i}) \times C_2(A))^2}{C_{TOT,i} \times C_2(A) + C_{random,i} \times C_{2r}(A)} \tag{18}$$

The NECR curves for mouse and rat phantoms are plotted in Figure 4 for 1, 3 and 6 ns coincidence windows. The NECR decreases at high activity because of the requirement of having two photons in the coincidence window. The scatter fractions (SF), peak true counting rate $(R_{t,peak})$, peak noise equivalent count rate $(R_{NEC,peak})$, activity at which $R_{t,peak}$ is reached, and activity at which $R_{NEC,peak}$ is reached can be found in Table 3 for mouse and rat phantoms and the three coincidence windows with an energy window of [450,600] keV.

3.3. Spatial Resolution

Spatial resolution was measured using the ^{22}Na point source, of diameter 0.25 mm, embedded in a 1 cm^3 acrylic cube. A total of 50 million ^{22}Na decays were simulated and an energy window of [450, 600] keV was used. It was assumed that the source activity would be low enough that random coincidences could be ignored. The source
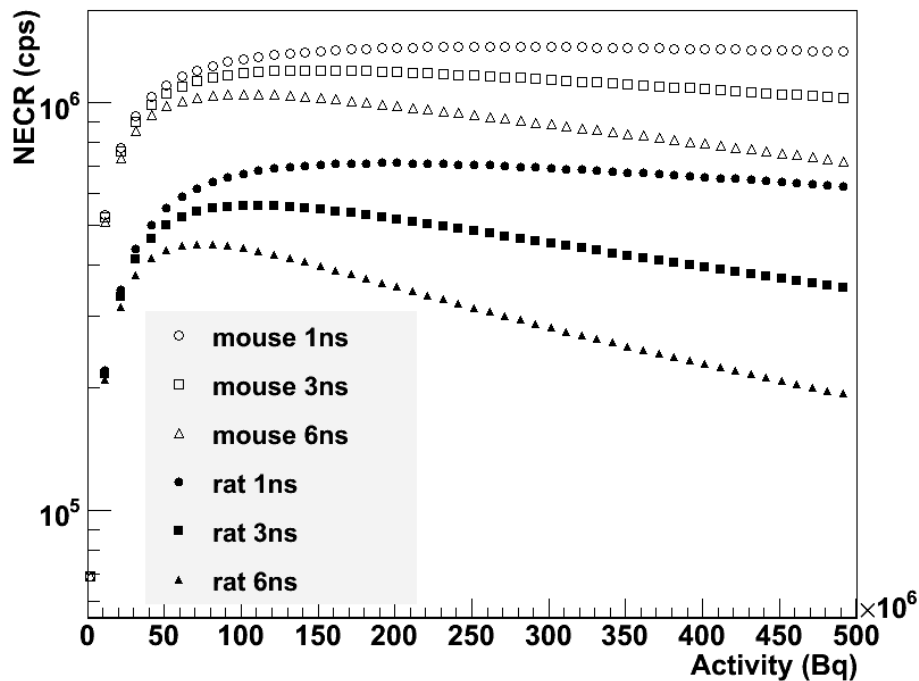
Figure 4: NECR vs. total activity, for mouse and rat phantoms and coincidence windows of 1, 3, and 6 ns. The dead time was 0.2 μs and the energy window was [450,600] keV.

Table 3: Scatter fraction and count rate performance for rat and mouse phantoms. The dead time was 0.2 μs and the energy window was [450,600] keV.

Phantom	Coincidence Window (ns)	SF (%)	$R_{t,peak}$ (kcounts)	$R_{NEC,peak}$ (kcounts)	$A_{t,peak}$ (MBq)	$A_{NEC,peak}$ (MBq)
Rat	1	20.8	920	712	212	192
	3		740	560	122	112
	6		606	451	82	72
Mouse	1	12.1	1570	1372	282	262
	3		1381	1202	162	152
	6		1212	1050	112	102

was placed at two axial positions: 0 and 12.5 mm. Five radial positions were used for each axial position: 0, 5, 10, 15 and 25 mm. The data were reconstructed with the list-mode MLEM iterative method (voxel size 0.15 x 0.15 x 0.15 mm, 20 iterations). The point spread functions were formed by summing one-dimensional profiles parallel to the direction of measurement and within two FWHM of the orthogonal directions. The FWHM and FWTM values were calculated through linear interpolation between adjacent pixels at one-half and one-tenth of the peak value in each direction. The point spread function for a point source at the CFOV is shown in Figure 5.

Radial, tangential and axial resolutions, reported as FWHM and FWTM, are given in Figures 6 - 7. At the CFOV radial, tangential, and axial FWHM resolutions of
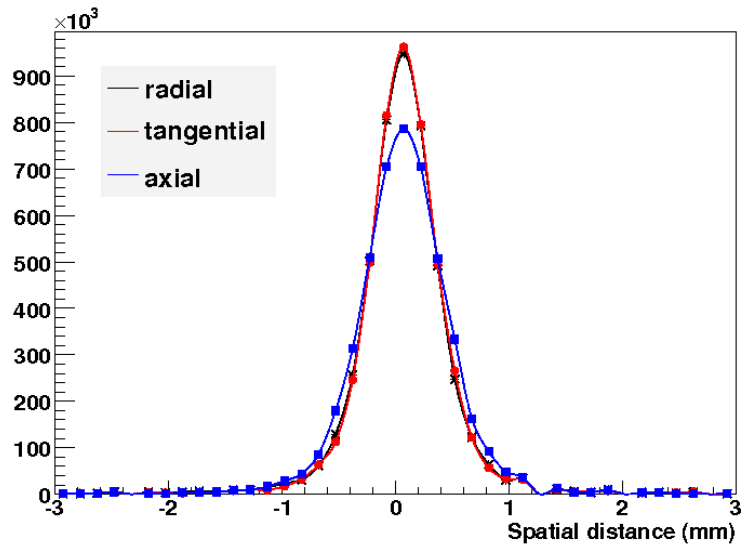
Figure 5: Point spread function in radial, tangential, and axial directions of a ^{22}Na point source at CFOV reconstructed with list-mode MLEM. Radial, tangential, and axial resolutions (FWHM) were 0.6 mm, 0.6 mm, and 0.8 mm.

0.6, 0.6, and 0.8 mm were found. At 25 mm radial and 12.5 mm axial offset, radial, tangential, and axial FWHM resolutions were 0.7, 0.7, and 0.8 mm. The results show a uniform resolution $<= 0.8$ mm (FWHM) throughout the FOV in radial, tangential, and axial directions. Due to the high resolution, efficiency, and solid angle coverage of the LXePET scanner, the reconstruction of the image from unrebinned 3D data using a 3D FBP was computationally too expensive whereas the reconstruction with 2D FBP algorithms led to a degradation of the axial resolution caused by the rebinning method. At the CFOV the 2D FBP gave the same results of the MLEM algorithm.

3.4. Image Quality Study

Figure 8 shows a trans-axial slice (thickness 24 mm) of the micro-Derenzo phantom with cylindrical rods of length 30 mm and diameters 1.6, 1.4, 1.2, 1.0, 0.8, and 0.6 mm reconstructed with the list-mode MLEM method (100 iterations). The voxel size was 0.15 x 0.15 x 0.15 mm. No attenuation or scatter corrections were applied. It was assumed that the source activity would be low enough that random coincidences could be ignored. Rods of diameter 0.6 mm to 1.6 mm are visible.

4. Conclusion

The potential imaging performance of a high resolution liquid xenon preclinical PET system was evaluated with Monte Carlo simulations. An event reconstruction algorithm was developed to handle multiple photon scatterings in liquid xenon, enabling us to refine the line of response selections and reduce the event mispositioning introduced
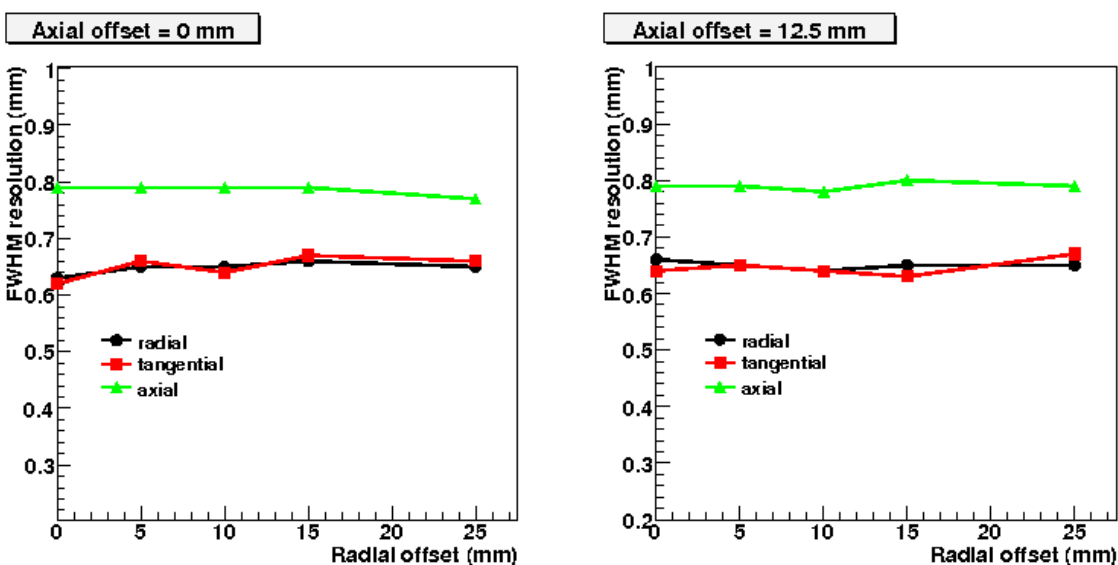
Figure 6: Radial, tangential, and axial resolution (FWHM) of a ^{22}Na point source reconstructed with list-mode MLEM.
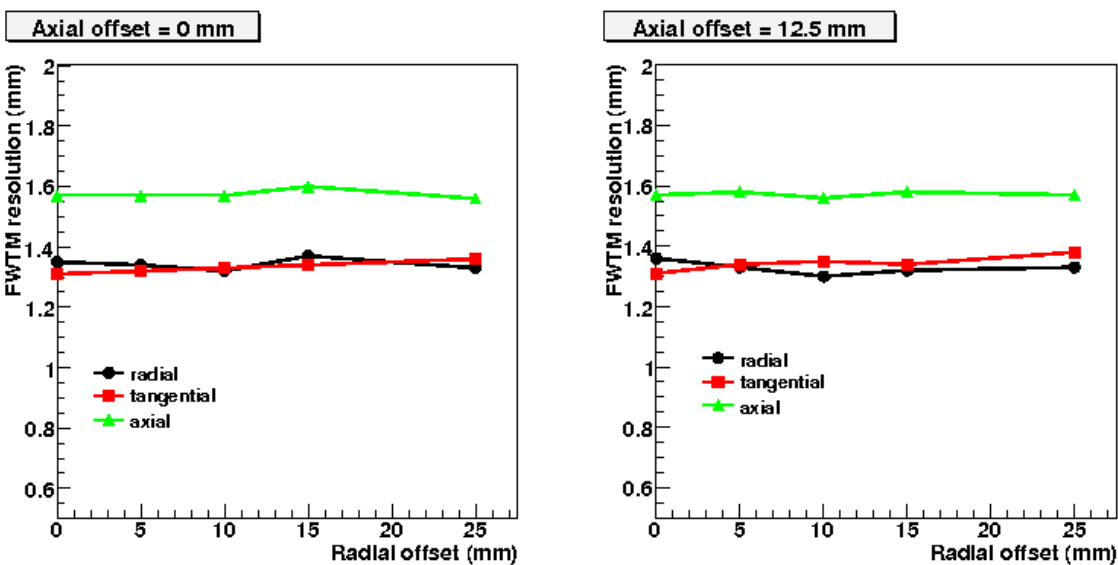

Figure 7: Radial, tangential, and axial FWTM of a ^{22}Na point source reconstructed with list-mode MLEM.

by scattered and random events which result in background noise. Using an energy window [450, 600] keV which is possible due to the high energy resolution, the results show that the LXePET system combines uniform high resolution radial, tangential, and axial position measurements throughout the field of view ($\leq$0.8 mm FWHM) with high sensitivity (12.6% at CFOV) and the ability to reject scatter and random coincidences. The scatter fraction was found to be 20.8%(12.1%), with associated peak NECR values of 1372 kcps at 262 MBq (712 kcps at 192 MBq) for mouse (rat)-like phantoms. These
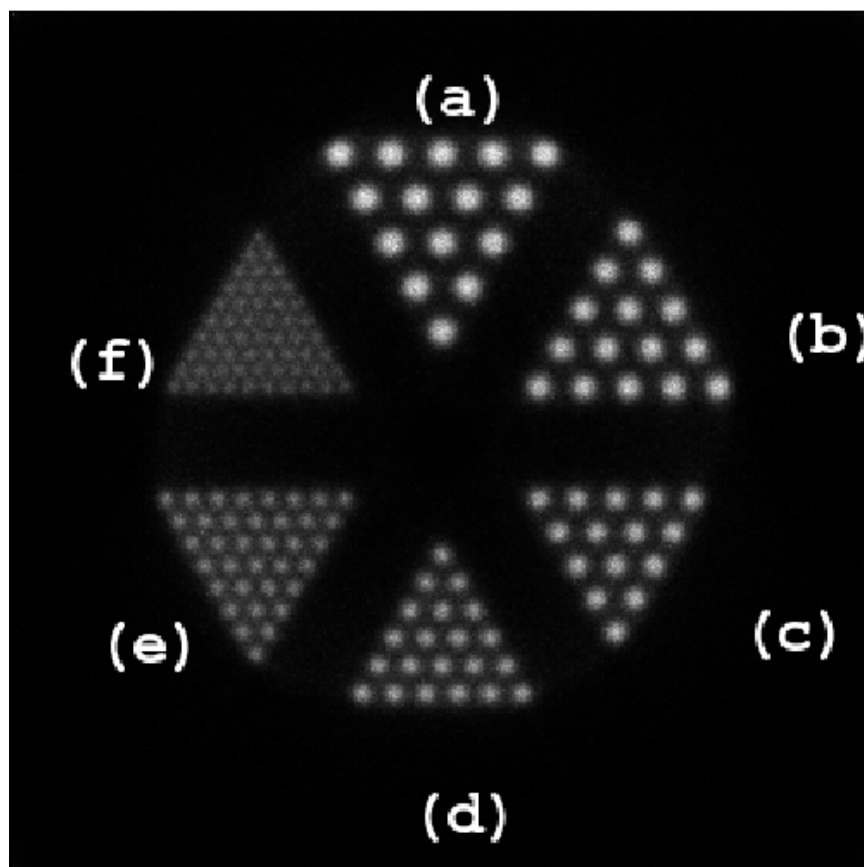
Figure 8: Micro-Derenzo phantom reconstructed using MLEM. Rod-to-rod separation is twice the rod diameter. Rod diameters: a (1.6mm), b(1.4mm), c(1.2mm), d(1.0mm), e(0.8mm), f(0.6mm).

results show the excellent imaging capabilities of the LXePET systems. Weighting schemes, where all available data are kept but each LOR is assigned a weight between 0 and 1, and filtering methods based on test statistic score computed with Compton kinematics will be investigated to further decrease noise in the images. Measurements are in progress to demonstrate the performance of the LXePET system described here.

Acknowledgments

References

[1] M. Bergeron, J. Cadorette, J.-F. Beaudoin, M.D. Lepage, G. Robert, V. Selivanov, M.-A. Tetrault, N. Viscogliosi, J.P. Norenberg, R. Fontaine, and R. Lecomte. Performance Evaluation of the

LabPET APD-Based Digital PET Scanner. *Nuclear Science, IEEE Transactions on*, 56(1):10 –16, 2009.

[2] Y. Tai, A. F. Chatziioannou, Y. Yang, R. W. Silverman, K. Meadors, S. Siegel, D. F. Newport, J. R. Stickel, and S. R. Cherry. MicroPET II: design, development and initial performance of an improved microPET scanner for small-animal imaging. *Phys. Med. Biol.*, 48(11):1519–1537, 2003.

[3] P. Sempere Roldan, E. Chereul, O. Dietzel, L. Magnier, C. Pautrot, L. Rbah, D. Sappey-Marinier, A. Wagner, L. Zimmer, M. Janier, V. Tarazona, and G. Dietzel. Raytest ClearPET(TM), a new generation small animal PET scanner. *Nucl. Instr. and Meth. A*, 571(1-2):498 – 501, 2007.

[4] J. N. Marx et al. The Time Projection Chamber. *Phys. Today*, 31N10:46, 1978.

[5] V. Chepel et al. Purification of Liquid Xenon and Impurity Monitoring for a PET Detector. *Nucl. Instr. and Meth. A*, 349:500–505, 1994.

[6] E. Conti et al. Correlated Fluctuations between Luminescence and Ionization in Liquid Xenon. *Phys. Rev. B*, 68:054201, 2003.

[7] M. Moszynski, M. Szawlowski, M. Kapusta, and M. Balcerzyk. Large area avalanche photodiodes in scintillation and X-rays detection. *Nucl. Instr. and Meth. A*, 485(3):504 – 521, 2002.

[8] E. Aprile et al. Observation of Anti-correlation between Scintillation and Ionization for MeV Gamma-Rays in Liquid Xenon. *Phys. Rev. B, Issue 1*, 76:014115.

[9] P. Amaudruz, D. Bryman, L. Kurchaninov, P. Lu, C. Marshall, J.P. Martin, A. Muennich, F. Retiere, and A. Sher. Simultaneous Reconstruction of Scintillation Light and Ionization Charge Produced by 511 keV Photons in Liquid Xenon: Potential Application to PET. *Nucl. Instr. and Meth. A*, 607:668–767, 2009.

[10] *NEMA Standards Publication NU4-2008: Performance Measurements of Small Animal Positron Emission Tomographs.* National Electrical Manufacturers Association, Rosslyn, VA, 2008.

[11] S. Agostinelli et al. G4–a simulation toolkit. *Nucl. Instr. and Meth. A*, 506(3):250 – 303, 2003.

[12] A. Miceli, P. Amaudruz, F. Benard, D. Bryman, L. Kurchaninov, J. P. Martin, A. Muennich, F. Retiere, T. J. Ruth, V. Sossi, and A.J. Stoessl. Liquid Xenon Detectors for Positron Emission Tomography. *Journal of Physics: Conference Series*, in-press, arXiv:1104.1458v1.

[13] E. Aprile, A. Curioni, K.L. Giboni, M. Kobayashi, U.G. Oberlack, and S. Zhang. Compton imaging of MeV gamma-rays with the Liquid Xenon Gamma-Ray Imaging Telescope (LXeGRIT). *Nucl. Instr. and Meth. A*, 593(3):414 – 425, 2008.

[14] U.G. Oberlack et al. Compton Scattering Sequence Reconstruction Algorithm for the Liquid Xenon Gamma-Ray Imaging Telescope (LXeGRIT). *arXiv:astro-ph/0012296*.

[15] G. Pratx, S. Surti, and C. Levin. Fast List-Mode Reconstruction for Time-of-Flight PET Using Graphics Hardware. *Nuclear Science, IEEE Transactions on*, 58(1):105 –109, 2011.

[16] F. Lamare, M. J. Ledesma Carbayo, T. Cresson, G. Kontaxakis, A. Santos, C. Cheze Le Rest, A. J. Reader, and D. Visvikis. List-mode-based reconstruction for respiratory motion correction in PET using non-rigid body transformations. *Physics in Medicine and Biology*, 52(17):5187, 2007.

[17] A. Rahmim, J.-C. Cheng, S. Blinder, M.-L. Camborde, and V. Sossi. Statistical dynamic image reconstruction in state-of-the-art high-resolution PET. *Physics in Medicine and Biology*, 50(20):4887, 2005.

[18] L. A. Shepp and Y. Vardi. Maximum Likelihood Reconstruction in Positron Emission Tomography. *IEEE Transactions on Medical Imaging*, 1:113–122, 1982.

[19] H. H. Barrett, T. White, and L. C. Parra. List-Mode Likelihood. *J. Opt. Soc. Am. A*, 1997.

[20] L. Parra and H. H. Barrett. List-Mode Likelihood: EM Algorithm and Image Quality Estimation demonstrated on 2D PET. 17:228–235, 1998.

[21] A. Rahmim, T.J. Ruth, and V. Sossi. Study of a convergent subsetized list-mode EM reconstruction algorithm. *Nuclear Science Symposium Conference Record, 2004 IEEE*, 6:3978 – 3982, 2004.

[22] M. Hudson and R. Larkin. Accelerated Image Reconstruction using Ordered Subsets of Projection

Data. *IEEE Trans. Med. Imag*, 13:601–609, 1994.